Chapter 5: Modeling Bone as a Two-Phase Composite

Fundamental finite element models are constructed for mineralized tissues at the ultrastructual length-scale to examine the basic composite mechanics and structure-properties linkages. The effects of mineral volume fraction, mineral particle aspect ratio, and phase continuity are examined. Issues associated with the sensitivity of models to input properties, such as modulus values of the component phases, are examined. An emphasis is on understanding how the observed mechanical response of mineralized tissues indirectly inform us as to their ultrastructure.

5.1 Mineralized Tissues as Composite Materials

Mineralized tissues have been considered as organic-inorganic composites in many different papers, most notably the work of Katz [1971]. Katz concluded that the simple examination of elastic modulus bounds based on phase fractions and component moduli resulted in adequate prediction of enamel properties but absolutely did not result in predictive capability for bone (Figure 5-1). The modulus of bone increases dramatically at nearly constant mineral volume fraction (in the region of mineral volume fraction 0.35-0.5). The result is that bone modulus spans a region between the upper and lower Hashin-Shtrikman composite bounds, and therefore cannot be predicted based on the mineral volume fraction alone [Katz, 1971].

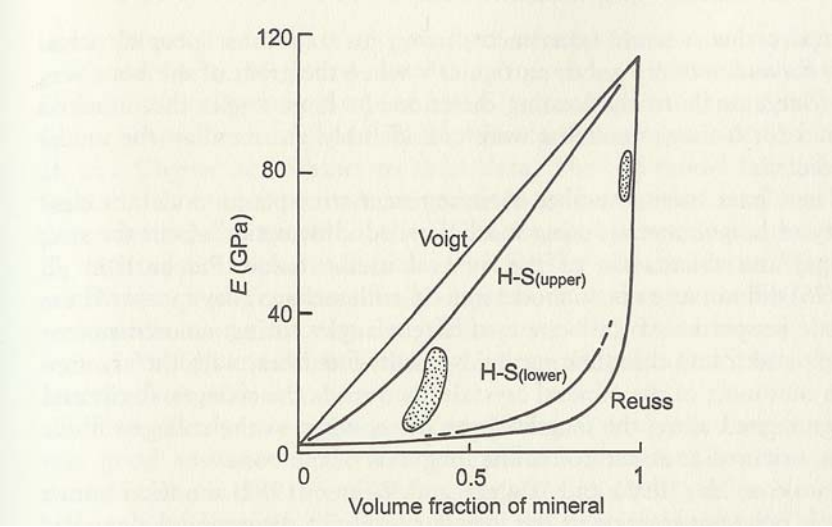

Figure 5-1: Elastic modulus bounds for different mineral volume fractions. The bone data (shaded region near volume fractions of 0.4) span a region between the upper and lower bounds, while enamel data (shaded region in upper right) lies along the lower bound. Figure from Currey [2002] after Katz [1971].

There has been recent renewed interest in modeling bone and other mineralized tissues as composite materials. In particular, a series of recent bone and dentin models utilizing a compliant matrix with stiff, high aspect-ratio particles have been introduced [Jager and Fratzl, 2000; Kotha and Guzelsu, 2002; Qin and Swain, 2004]. One

contrasting model has been introduced, in which the mineral phase is assumed to be continuous [Hellmich and Ulm, 2002].

Critical examination of the literature reports of models utilizing soft matrices with high AR stiff particles for bone demonstrate that some assumptions made in the modeling may be responsible for the apparent good results of this approach in stark contrast to the findings in this study. For example, Jager and Fratzl [2000] assume the particles are rigid while Kotha and Guzelsu [2002] model the matrix as having a modulus of 1.2 GPa even though modulus values an order of magnitude less have been reported for demineralized bone [Catanese et al, 1999].

The existing composite-based ultrastructural models for bone will be examined here within a single finite element (FE) modeling framework, in which a large variety of parameters will be examined. In doing so, a number of hypotheses proposed in the literature for the ultrastructure of bone, and specifically the factors contributing to the elastic modulus of bone such as high aspect-ratio particles and phase continuity, will be examined within this unified FE framework.

The information necessary for examination of mineralized tissues within a simple composite materials framework is twofold: knowledge of the elastic properties of the individual phases, and knowledge of the relative proportions of different phases (e.g. their phase fractions) present in the composite material. As was discussed in the first chapter of this work, it is known that the mineral phase is a carbonated apatite (hydroxyapatite or dahllite) and that the remainder of the material is water and organic (mainly protein) phases. For a first approximation, mineralized tissues are considered as a two phase composite of mineral and non-mineral phases. I begin by examining the composition and phase fractions of mineral and non-mineral phases within mineralized tissues (bone, dentin, enamel).

5.1.1 Mineral Volume Fractions

Compositions of mineralized tissues are frequently reported in terms of weight

(Table 1). From the weight fraction of mineral, a volume fraction for the mineral and non-mineral phases can be calculated (Eqn. 2-45). These estimates can then be compared with estimates made based on the material densities (ρ_i) using a rule of mixtures approach (Eqn. 2-44). In both cases, the density of the apatite mineral phase is taken to be 3.1 g/cm^3 [Deer et al, 1966] and the density of the remainder (organic phase and water) is assumed to be unity.

Table 5-1: Mineralized tissue mean composition by weight or by mass density

	Weight percents [Currey, 2002]			***Mass Density (g/cm^3)***
%	***Water***	***Mineral***	***Organic***	
Bone	5-10	75	15-20	1.8-2.0
Enamel	2	97	1	2.97
Dentin	10	70	20	2.14

Calculated mineral volume fractions for each tissue, obtained using the composition data from Table 5-1, are presented in Table 5-2. The calculations differ slightly, particularly in the composition of dentin relative to that of bone, but the mineral volume fractions from either calculation are comparable. The reported volume fraction of mineral in bone is approximately 50% [Hayes, 1991] in good agreement with either calculation. For simplicity here, most finite element simulations of bone or dentin will assume a volume fraction of 50% mineral, in good agreement with either calculation for both materials (Table 5-2).

Table 5-2: Mineralized tissue volume fraction estimated in two ways and based on raw data in Table 5-1.

	V_f from Weight % mineral	***V_f from mass density***
Bone	0.49	0.38-0.48
Enamel	0.91	0.94
Dentin	0.43	0.54

Having established reasonable estimates of the phase fractions for composite modeling purposes, attention turns to the component elastic moduli.

5.1.2 Mineral Phase Elastic Properties

As was discussed briefly in Chapter 1, biological apatite is an analog of mineral apatite, and so it's mechanical properties are quite well known. In addition, the elastic modulus under indentation conditions was examined in Chapter 3 for mineralogical (fluoro-) apatite in single crystal form and in Appendix A for nanocrystalline (hydroxy-) apatite prepared using a biomimetic process. The indentation modulus is particularly useful for finite element calculations since the anisotropy is averaged as a result of the indentation measurement, and an approximate isotropic modulus can be considered. Based on the results shown in Chapter 3, the plane strain modulus (E') of crystalline biomineralized apatite was on average 160 ± 7 GPa and that of mineral apatite was 155 ± 4 GPa. Assuming that the Poisson's ratio for both is approximately the mineral apatite value of 0.28-0.30, the elastic modulus for apatite can be taken as 145 GPa. In fact, over a reasonable range of Poisson's ratio (0.2 to 0.35), the modulus of fully-dense apatite can be taken with some certainty to be 140-150 GPa. These values are slightly larger than those reported by Katz and Ukraincik [1971], of 112 GPa for hydroxyapatite and 120 GPa for fluoroapatite.

A separate question arises as to the density of the mineral in platelet-form in mineralized tissues. Mineral that is not fully dense will inevitably have an elastic modulus less than that obtained for fully-dense apatite, and this is an open question [Qin and Swain, 2004]. A value of 100 GPa will be used for most of the FE modeling presented in this work.

5.1.3 Organic Phase Elastic Properties

The issue of selecting an appropriate elastic modulus for the organic (collagen-

water) phase is far more complicated than for apatite. Literature modulus values are wide-ranging, depending on the technique used and the source of collagen. Most modeling for mineralized tissues has incorporated a modulus of 1-1.5 GPa [Wagner and Weiner, 1992; Akiva et al, 1998 ; Kotha and Guzelsu, 2002; Qin and Swain, 2004]

Cusack and Miller [1979] used Brillouin light scattering and obtain an elastic modulus value of 11.9 GPa for dry collagen and 5.1 GPa for wet collagen. The extremely large values are probably due to the ultra-high frequency (10^{10} Hz) nature of the measurement since collagen is viscoelastic and measured (complex) modulus in a viscoelastic solid depends strongly on the measurement frequency. These values, therefore, would not be appropriate for the quasistatic elastic modeling of mineralized tissues.

Two recent works [An et al, 2004; Freeman and Silver, 2004] discussed the advances in measuring fundamental collagen elastic properties, taking advantage of technological developments such as the optical tweezers and sophisticated computational techniques. Both of these works report extremely low modulus values for collagen at molecular scales, in the single- to double-digit MPa range. Both works also note the increased elastic modulus values for larger structural units of collagenous soft tissues, such as whole tendons, typically in the hundreds of MPa to single-digit GPa range. This increase in modulus for larger structural units is attributed to cross-linking [Freeman and Silver, 2004]. A comparison of the approximate stress-strain for four different hierarchical levels of collagen from [An et al, 2004] is shown in Figure 5-2.

Also of interest in the discussion of stress-strain behavior of collagen is the nonlinear nature of the material response, as shown in Chapter 1 (Figure 1-14). The perceived elastic modulus can be extremely strain-level dependent, something that has been deliberately excluded from the data shown in Figure 5-2, but is of concern in modeling. For linearly elastic finite element models, the strain levels are small by definition and therefore the modulus of interest is that at small strains, not the maximum value at large (near-failure) strains. Based on all of these factors, the baseline elastic modulus taken for collagen in this work is 100 MPa, consistent with the demineralized

bone data in Figure 1-14 for strain levels less than 2%, consistent with intermediate hierarchy scales in Figure 5-2, and lower than the maximum reported values for whole tendons (~ 1.5 GPa). The sensitivity of modeling results to selected collagen modulus will be discussed later in this chapter. Values of both 100 MPa and 1 GPa will be used in the modeling analysis of current work.

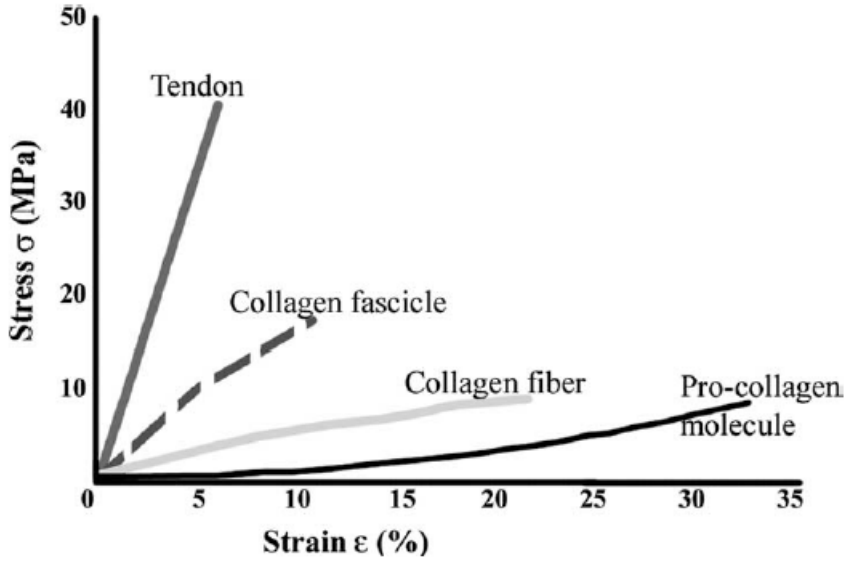

Figure 5-2: Stress-strain (σ-ε) plot for four different levels of collagen hierarchical organization [figure from An et al, 2004]. The approximate (secant) elastic modulus for each line on the plot gives tendon *E* = 636 MPa, collagen fascicle *E* = 162 MPa, collagen fiber *E* = 43 MPa, and pro-collagen molecule *E* = 27 MPa.

For modeling purposes, the Poisson's ratio of both phases will be fixed at values at 0.3. This value is in good agreement with the $\nu = 0.28$ reported for apatite [Katz and Ukraincik, 1971] and the $\nu = 0.3$ reported for bone [Zysset et al, 1999].

5.2 FEA Model for Homogeneous Loading

A plane strain finite element model was constructed to examine structural details of mineralized tissues at the ultrastructure level. The finite element (FE) model was constructed in 2D using FlexPDE (PDE Solutions, Antioch, CA) to represent a two-phase composite with circular inclusions in the plane, where the circle radius (*r*) was 30 nm. The "particles" were circles and were arranged in a square array with interparticle spacing (*b*) a fixed multiple of the particle radius to vary the area fraction (and in turn the plane strain volume fraction) for each phase, as shown in Table 5-3. The model incorporated 200 particles, in 10 rows of 20 columns. The elastic modulus of the compliant (gelatin/collagen) phase was assumed to be 100 MPa and that of the stiff (hydroxyapatite) phase was set to 100 GPa. Poisson's ratio was assumed to be 0.3 for both phases. Models were constructed with both the stiff (apatite) and compliant (gelatin) phases as the continuous (non-particle) phase.

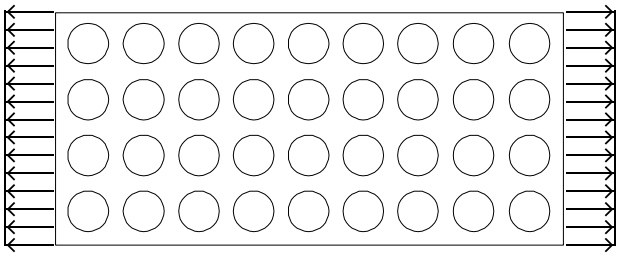

Figure 5-3: Finite element model of two-phase composite, homogeneously loaded in plane strain by equal and opposite tensile deformations applied to each end.

Table 5-3: 2D area fraction (equal to 3D volume fraction for plane strain) calculated for FEA meshes with different particle spacing

particle spacing (b), in terms of particle radius, r	*Continuous phase*	*Area fraction stiff (apatite) phase*
2.2 r	compliant	0.65
	stiff	0.35
2.5 r	compliant	0.5
	stiff	0.5
3 r	compliant	0.35
	stiff	0.65
4 r	compliant	0.2
	stiff	0.8
5 r	compliant	0.13
	stiff	0.87
6 r	compliant	0.09
	stiff	0.91
20 r	compliant	<0.01
	stiff	>0.99

Homogeneous plane strain loading was modeled for the composite and for a homogeneous apatite material. A uniform *x*-displacement perturbation was applied to each end (*e.g*. face with *x*-direction normal) with magnitude equal to the particle radius *r*, as schematically illustrated in Figure 5-3.

The plane-strain stress-strain relationship

$$\sigma_x = \frac{E}{(1-\nu^2)}\epsilon_x \qquad [5\text{-}1]$$

was used to validate the quantitative nature of the homogeneous model (E = 100 GPa) where the applied strain $\epsilon_x = 2r/w$ and w is the model width. Stress (σ_x) from the FEA

computation was found to be uniform and equal to the predicted value.

The *x*-stress $(\sigma^{\text{composite}})$ on the edges resulting from the displacement perturbation was integrated across the edge to obtain the load per depth or line load $(P_{\text{L}}^{\text{composite}})$. The same process was repeated for the corresponding homogeneous FE model with $E = 100$ GPa, integrating the stress (σ^{100}) to get the load (P_{L}^{100}) for each geometrical configuration and identical applied loading conditions. The loads were used in a scaling relationship to compute the effective elastic modulus for the composite:

$$E_{\text{EFF}} = \frac{P_{\text{L}}^{\text{composite}}}{P_{\text{L}}^{100}} 100\,\text{GPa} \qquad [5\text{-}2]$$

Figure 5-4 shows as open symbols the effective elastic modulus (Eqn. 5-2) for a series of tensile-loaded FE models with varying particle spacing (from 2.5*r* to 20*r*) and thus varying particle volume fraction (Table 5-3). Also in Figure 5-4 are the Voigt-Reuss bounds (V-R, Eqn. 2-40 and 2-41) and Hashin-Shtrikman bounds (H-S, Eqn. 2-43 and 2-44). The effective elastic modulus from tensile uniform loading FEA of composite materials showed good agreement with the Hashin-Shtrikman (H-S) bounds (Figure 5-4) even for particle volume fractions of more than 50%. The compliant phase-continuous models followed the lower H-S bound and the stiff phase-continuous models followed the upper H-S bound. Interestingly, the upper bound values, 20-30 GPa for mineral volume fractions 0.35-0.5, are consistent with modulus values seen for mineralized tissues, while the lower bound values for the same mineral fractions are 200-300 MPa, much too low to represent the elastic modulus of bone.

The results of this preliminary modeling exercise suggest that the apatite phase may be acting as the functional matrix material in bone and related materials. The suggestion of mineral matrix functionality was also made recently by Hellmich and Ulm [2002] based on energetics arguments, and is consistent with the observations in Gray's Anatomy (section 1.2.2.3). However, most models for bone have considered the

composite material as a compliant matrix with stiff reinforcement [Jager and Fratzl, 2000; Kotha and Guzelsu, 2002].

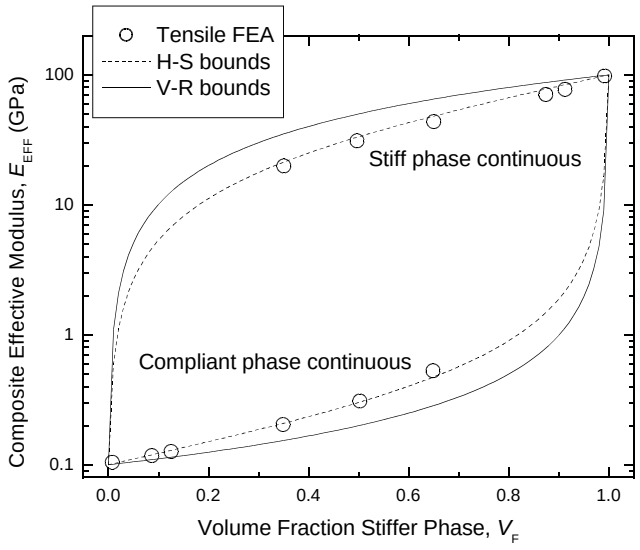

Figure 5-4: Composite effective elastic modulus (E_{EFF}) as a function of stiff phase volume fraction (V_f) computed for FE tensile loading of composites

One potential difference between previously reported composite models of bone and the current simulations, which may affect the conclusions about phase continuity, was the particle geometry. The current section used idealized circular (symmetric) particles. Next, high aspect-ratio particles are examined.

5.3 Anisotropy: Particle Shape and Distribution Variations

Clearly there is a disconnect between an idealized model with circular particles and the microstructure of mineralized tissues, with plate-like or needle-like mineral particles. In this next series of models, the effect of mineral particle anisotropy is explored, and comparisons are made with the measured anisotropy of mineralized tissues. Similarities and differences between the current study and previous bone composite models are discussed. The likelihood of high particle aspect ratio as a dominant mechanism of bone stiffening will be discussed.

5.3.1 Anisotropy Model

Hydroxyapatite mineral particles in bone are considered to be plates or needles, with a non-unity aspect ratio [Currey, 2002]. It has been suggested that the mineral aspect ratio is critical in determining the composite material modulus for bone [Gao et al, 2003]. Therefore, the effect of particle aspect ratio on composite response was next investigated.

Particles were rectangles 80 nm in width (w) and with heights decreasing from 80 nm based on the particle aspect ratio (AR) as shown in Figure 5-5(a). Particle aspect ratio (AR = w/h) was set to 1, 2, 4, 8, 16, or 32. Initially the same square array used for the spherical particles was employed but additional models were constructed with a staggered particle array consistent with those used by other investigators, as shown in Figure 5-5(b). The volume fraction (V_f) was fixed at 50% for each phase in most models. Two interparticle spacings were defined in directions parallel (s_1) and perpendicular (s_2) to the long axis of the particles. Interparticle spacings (s_i) were adjusted to maintain fixed volume fraction for conditions of identical or different interparticle spacings in the 1- and 2-directions (Figure 5-5(c)). The models included 150-200 particles.

The elastic modulus of the compliant (gelatin or collagen) phase was initially assumed to be100 MPa but 1 GPa was used for a limited set of simulations to examine

the effect of compliant phase modulus. The modulus of the stiff (hydroxyapatite) phase was set to 100 GPa. Poisson's ratio (ν) was assumed to be 0.3 for both phases. Models were constructed with both the stiff (mineral) and compliant (collagen) phases as the continuous (non-particle) phase.

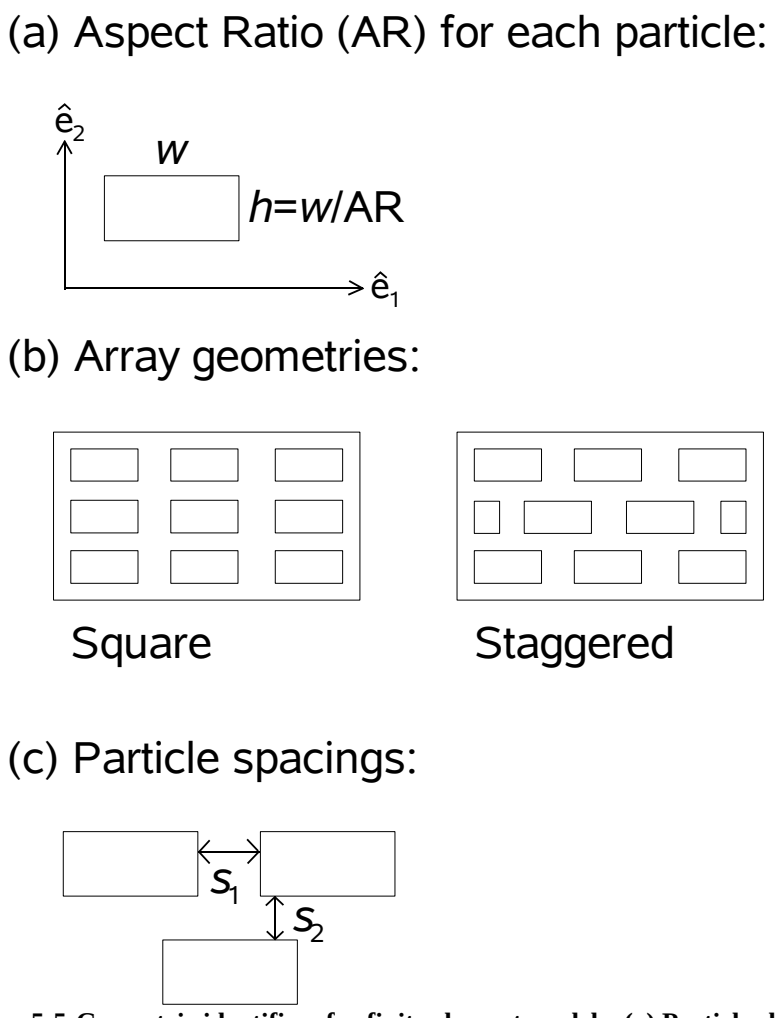

Figure 5-5:Geometric identifiers for finite element models: (a) Particle shape defined in terms of aspect ratio (AR) and 1-2 coordinate system defined parallel and perpendicular to the particle long axis; (b) particle array geometries as square or staggered; (c) interparticle spacings in directions parallel (s_1) and perpendicular (s_2) to the particle long axis.

Effective modulus parallel to the particle long axis was denoted E_1 and perpendicular to the long axis was denoted E_2. Composite moduli in each direction

relative to the particle axes were examined as a function of stiff phase volume fraction (V_f), particle geometry, and particle arrangement. A summary of the combinations of parameters examined in the current series of models is shown in Table 5-4.

Table 5-4: Summary of finite element simulations run in the current study. Each combination of parameters was examined for both stiff-phase continuity and compliant phase continuity.

Model group	Collagen (compliant phase) elastic modulus E_{coll}	particle array geometry	particle aspect ratios (AR)	volume fraction stiff (mineral) phase V_F	interparticle spacings (s_1, s_2)
(A)	100 MPa	square	1	varied	$s_1 = s_2$
(B)	100 MPa	square	1, 2, 4, 8, 16, 32	0.5	$s_1 = s_2$
(C)	100 MPa	staggered	1, 2, 4, 8, 16	0.5	$s_1 = s_2$
(D)	1 GPa	staggered	1, 2, 4, 8, 16	0.5	$s_1 = s_2$
(E)	100 MPa	square	2, 4, 8	0.5	$s_1 \neq s_2$

As with the circular particles, for square (AR = 1) particles in a square array, at different volume fractions (model group A), the FE results are in good agreement with the Hashin-Shtrikman bounds (Figure 5-6).

An interesting comparison on the direct effects of particle and arrangement can be made by comparing a set of circular and square (AR = 1) particles in square and staggered arrays (Table 5-5). For square particle arrays, elastic modulus results are approximately isotropic $(E_1 = E_2)$ regardless of the shape (circle or square) of the particles. This is consistent with the fact that the particle arrangement is symmetric for a square array. However, for a staggered (bricks and mortar) array, there is some anisotropy apparent even when the particles themselves are symmetric, due to the asymmetry of the array. This anisotropy effect is most pronounced for the stiff matrix model (and interestingly enough is quite similar to the observed anisotropy in bone, as discussed later in this work).

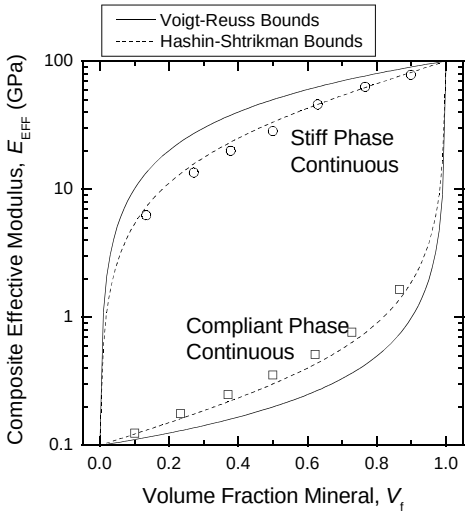

Figure 5-6: Effective elastic modulus as a function of mineral volume fraction for square arrays of square (AR = 1) particles (Table 5-4, model group A).

Table 5-5: Isotropy or anisotropy in FEA meshes with different particle geometries and arrangements

particle shape, array style	***continuous phase***	***E1 (GPa)***	***E2, (GPa)***	***ratio E1/E2***
circles, square array	stiff	30.88	30.47	1.01
	compliant	0.31	0.3	1.01
squares, square array	stiff	28.02	28.55	0.98
	compliant	0.35	0.36	0.99
squares, staggered	stiff	23.9	15.15	1.58
	compliant	0.31	0.38	0.81

In models with varying particle aspect ratios, the same trends in effective elastic modulus with particle aspect ratio were apparent in square and staggered arrays, and for cases of both compliant (100 MPa) and moderate (1 GPa) collagen elastic modulus (Figure 5-7). The longitudinal modulus (E_1) in stiff-phase continuous models was nearly

independent of particle aspect ratio, as was the transverse modulus (E_2) of compliant-phase continuous materials. The longitudinal modulus in compliant-phase continuous materials increased with particle aspect ratio, while the transverse modulus in stiff-phase continuous materials decreased with particle aspect ratio. The decrease in E_2 with aspect ratio for stiff-phase continuity was more pronounced in staggered particle arrays compared to square particle arrays. (Figure 5-7 (a) and (b)). The trends in behavior for the staggered arrays with different base collagen moduli were similar (Figure 5-7 (b) and (c)), though at large particle aspect ratios the difference between the compliant- and stiff-phase continuity models diminished substantially for smaller modulus mismatch (Figure 5-7(c)).

The anisotropy ratios (E_1/E_2) for six sets of models (from Figure 5-7, models from Table 5-4 B-D) are shown as a function of particle aspect ratio in Figure 5-8. Four of the six responses are quite similar, with the exceptions both being models with a stiff matrix and staggered compliant particles, which were more anisotropic than the other four models. As was noted above, this great anisotropy is due not to a change in modulus parallel to the particles but due to a decreased modulus in the transverse direction (Figure 5-7).

For compliant matrix models with an assumed collage modulus of 100 MPa, the elastic modulus parallel to the particles (E_1) does increase substantially with particle aspect ratio. However, for both square and staggered array models, even for particles with an aspect ratio of 16, the effective modulus in the 1-direction is not increased sufficiently to represent the properties of bone: the modulus was still a full order of magnitude too low (~ 2 GPa) compared to the experimental results of around 20-25 GPa for bone. In conjunction with this increase in E_1 the relative constancy of E_2 around 250 MPa does not recommend this model as having great promise for modeling the response of bone. When the collagen modulus is raised to 1 GPa, E_1 = 17 and E_2 = 2.5 GPa for AR = 16, closer to the expected range for bone but still demonstrating remarkable anisotropy of nearly an order of magnitude.

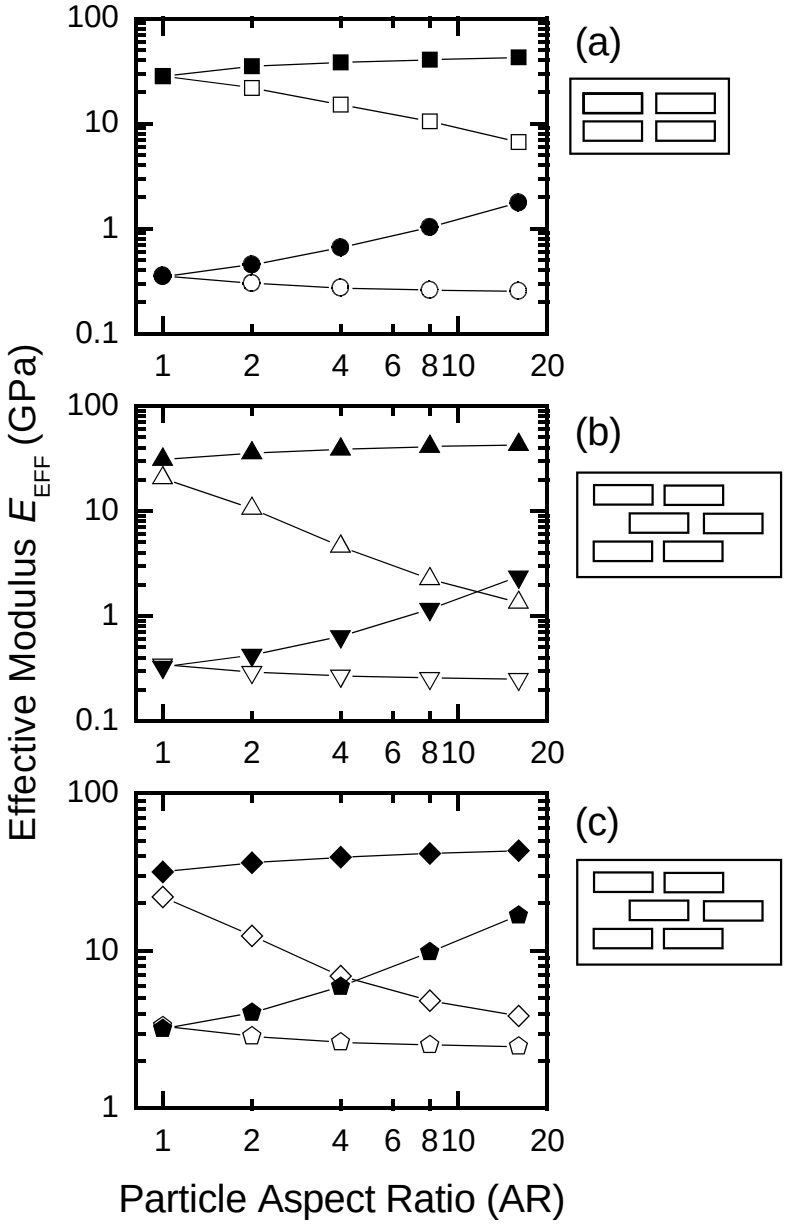

Figure 5-7: Effective composite elastic modulus (E_{EFF}) in directions parallel (1) and perpendicular (2) to the particle long axis for particles in a square (a) or staggered (b,c) array with varying aspect ratios (AR). Volume fraction of each phase was held fixed at 0.5 and the modulus ratio was 1000 (a,b) or 100 (c). Solid symbols: E_1; open symbols, E_2. Square symbols for models with mineral phase continuous; circle symbols for compliant-phase continuity.

For stiff matrix models, changing the particle aspect ratio did not substantially affect the E_1 modulus but the E_2 modulus was substantially diminished with increasing aspect ratio (Figure 5-7). This effect was even more dramatic in staggered particle arrays compared to square arrays. However, the transverse modulus is still in the GPa range and has not fallen to the MPa magnitude of the moduli seen in compliant matrix models. However, with large particle aspect ratios, the anisotropy as indicated by the modulus ratio is more than an order of magnitude.

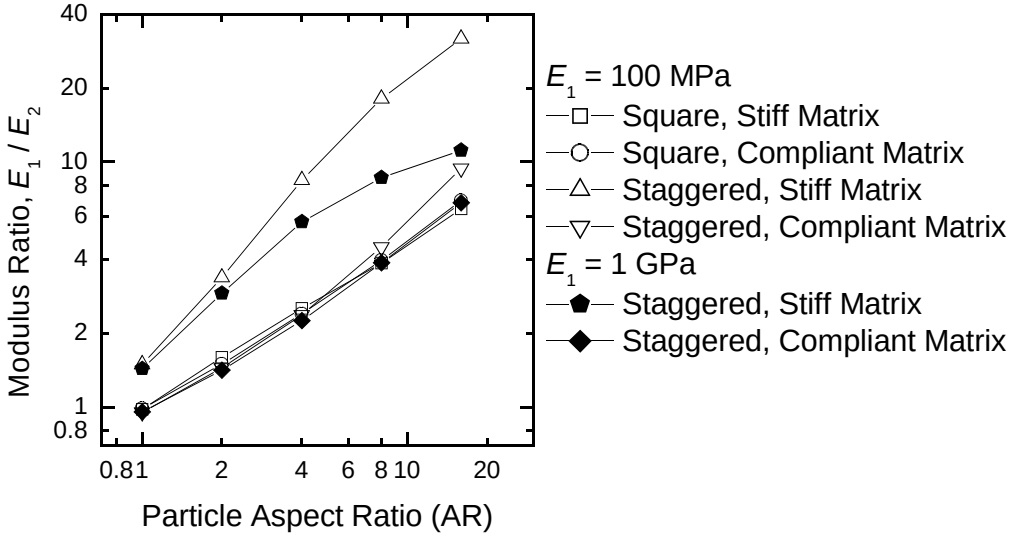

Figure 5-8: Anisotropy ratio (E_1/E_2) as a function of particle aspect ratio (AR) for finite element models with rectangular particles in square or staggered arrays.

For purposes of comparison, the anisotropy in femoral cortical bone has been measured, with individual moduli $E_{\text{longitudinal}} = 17\,\text{GPa}$ and $E_{\text{transverse}} = 11.5\,\text{GPa}$ [Hayes, 1991] giving an isotropy ratio $E_1/E_2 = 1.48$. Swadener [2001] gives the modulus anisotropy ratio for bone as $E_1/E_2 = 1.75$. This value corresponds to AR < 4 in the FEA simulations. Most bone is laminated with layers oriented in different directions, so the anisotropy ratio calculated from FEA should not be directly considered as contradictory

to experimental results. However, it is interesting to note that if the particles were truly functioning independently, with such large aspect ratios, the degree of anisotropy inherent in each subunit layer of bone would be quite substantial.

An additional problem with independent high aspect ratio particles is the potential for particle buckling under compression; bone is frequently loaded in bending in vivo, in which both tensile and compressive stresses and strains exist. A stiff matrix model has the potential to function well in both tension and compression with apatite buckling restricted by connectivity with surrounding particles.

5.3.2 FEA Comparison with Halpin-Tsai

The Halpin-Tsai relationships for composite materials are approximations to exact elasticity solutions in easy-to-calculate simple analytical forms. There are well-known Halpin-Tsai expressions for the elastic modulus of a composite with oriented short fibers or whiskers, precisely the situation being modeled with the FE analysis presented in this section. The analytical expressions for the longitudinal and transverse elastic moduli (E_L, E_T) relative to the compliant matrix modulus (E_m) are [Agarwal and Broutman, 1990]:

$$\frac{E_L}{E_m} = \frac{1+(2l/d)\eta_L V_f}{1-\eta_L V_f} \qquad [5\text{-}3]$$

$$\frac{E_T}{E_m} = \frac{1+2\eta_T V_f}{1-\eta_T V_f} \qquad [5\text{-}4]$$

where l/d is the particle aspect ratio, V_f is the volume fraction reinforcing phase and the coefficients η_L and η_T are related to the filler and matrix phase elastic moduli (E_f, E_m) as:

$$\eta_L = \frac{(E_f/E_m)-1}{(E_f/E_m)+2(l/d)} \qquad [5\text{-}5]$$

$$\eta_T = \frac{(E_f/E_m)-1}{(E_f/E_m)+2} \qquad [5\text{-}6]$$

The longitudinal and transverse modulus values have been calculated from expressions 5-3 to 5-6 for the compliant phase continuous models here (E_m = 100 MPa or 1 GPa, E_f = 100 GPa, AR = 1 to 16) and are shown in Figure 5-9 along with the FEA results presented in Figure 5-7. The shape of the FE modeling and analytical responses are identical, while the numerical results are shifted slightly. The Halpin-Tsai expressions are empirical and this reasonable but imperfect agreement is to be expected at intermediate volume fractions of reinforcement phase [Hull and Clyne, 1996].

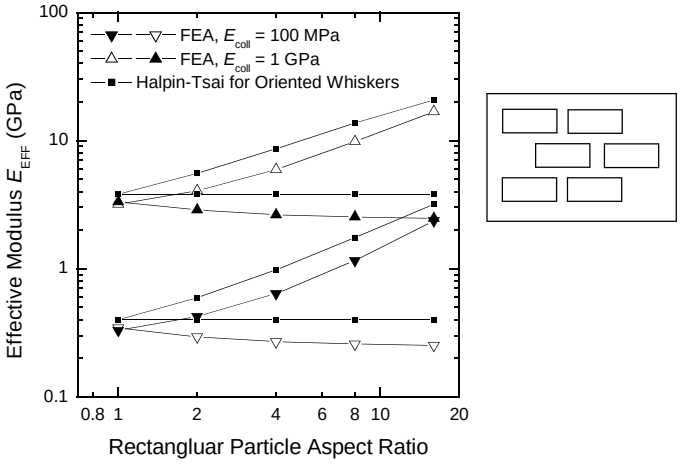

Figure 5-9: Effective elastic modulus (E_{EFF}) as a function of particle aspect ratio (AR). Results are compared for FEA (Figure 5-7) compared with Halpin-Tsai empirical expressions for whiskers (Eqns 5-3 to 5-6).

From the longitudinal and transverse modulus expressions, a random modulus can be calculated, assuming that the orientation changes in local domains (as is true for bone). The random elastic modulus is given by

$$E_{random} = 3/8\, E_L + 5/8\, E_T \qquad [5\text{-}7]$$

The shear modulus can also be approximated:

$$G_{\text{random}} = 1/8\, E_{\text{L}} + 1/4\, E_{\text{T}} \qquad [5\text{-}8]$$

and the combination of the elastic and shear moduli can be used to calculate a Poisson's ratio for the random composite:

$$\nu_{\text{random}} = \frac{E_{\text{random}}}{2G_{\text{random}}} - 1 \qquad [5\text{-}9]$$

The random modulus for the Halpin-Tsai expressions is shown as a function of particle aspect ratio in Figure 5-10 for collagen modulus values of 100 MPa and 1 GPa. At AR = 16, the value of E_{random} is around 10 GPa for collagen modulus of 1 GPa and just under 2 GPa for collagen modulus of 100 MPa.

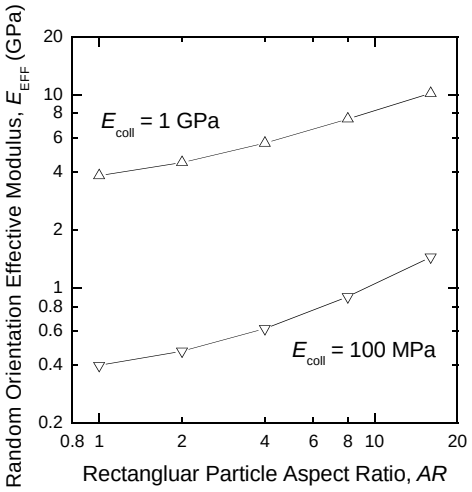

Figure 5-10: Calculated effective modulus (E_{EFF}) as a function of aspect ratio (AR) for a random orientation particulate composite, based on the Halpin-Tsai longitudinal and transverse modulus values (Eqn. 5-7).

The calculated Poisson's ratio for these same conditions (Eqn. 5-9) varied from 0.33 for particles with unity aspect ratio to 0.43 for AR = 16 and E_m = 1 GPa, or from 0.33 to 0.45 for AR = 1 to 16 and E_m = 100 MPa.

5.3.3 Examination of the Stiffening Mechanism in High-AR Composites

Discrete high-aspect ratio (AR) particles were able to provide some stiffening to a compliant matrix,but it was unclear what mechanism was controlling this phenomenon. Therefore a more detailed investigation of high AR particle composites was undertaken. In most previously presented models (section 5.3.1 above, and Table 5-4 A-D) the interparticle spacing was fixed to be identical in the 1- and 2-directions $(s_1 = s_2)$. This constraint resulted in geometries in which there were smaller interparticle spacings for high AR particles, leaving it unclear if it was the particle aspect ratio responsible for the stiffening effect or the interparticle spacing. New models were constructed (Table 5-4E) that allowed for different interparticle spacings in the 1- and 2-directions $(s_1 \neq s_2)$ to independently vary interparticle spacing in the direction of loading and particle aspect ratio.

Results for these models as well as those considered previously (section 5.3.1) were examined in the context of a "length fraction" of particles in the direction of loading:

$$L_P = \frac{w}{w + s_1} \quad \text{for loading in the 1-direction} \qquad [5\text{-}10]$$

$$L_P = \frac{h}{h + s_2} \quad \text{for loading in the 2-direction} \qquad [5\text{-}11]$$

The effective elastic modulus for a large series of models is plotted as a function of this "length fraction" parameter in Figure 5-11. The data lie on a universal curve.

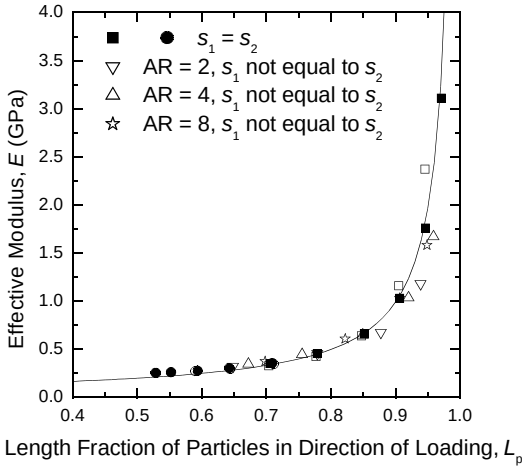

Figure 5-11: Effective elastic modulus (E) as a function of particle length fraction in the direction of loading (L_p) for square array particles with varying aspect ratios (AR = 1 to 32) and varying interparticle spacings (s_i). Includes data from Figure 5-7. Volume fraction (V_f) of each phase was held fixed at 0.5 with the modulus ratio (E_{min}/E_{coll} = 1000) and with the compliant phase continuous.

The equation for the universal curve was found to be the V-R lower bound, rewritten in terms of length fraction of particles:

$$\frac{1}{E_{\mathrm{EFF}}} = \frac{L_{\mathrm{P}}}{E_{\mathrm{min}}} + \frac{1-L_{\mathrm{P}}}{E_{\mathrm{coll}}} \qquad [5\text{-}12]$$

Therefore, interestingly enough the models previously presented for bone (Figure 5-12, [Jager and Fratzl, 2000; Gao et al, 2003]) as well as the Halpin-Tsai empirical equations for a whisker composite [Agarwal and Broutman, 1990], are perhaps misleading in presenting the elastic modulus as a direct function of particle aspect ratio. Particles of different aspect ratio can result in materials with equal modulus if the interparticle spacings in the direction of loading are adjusted to give equal length fractions (L_p) in the loading direction.

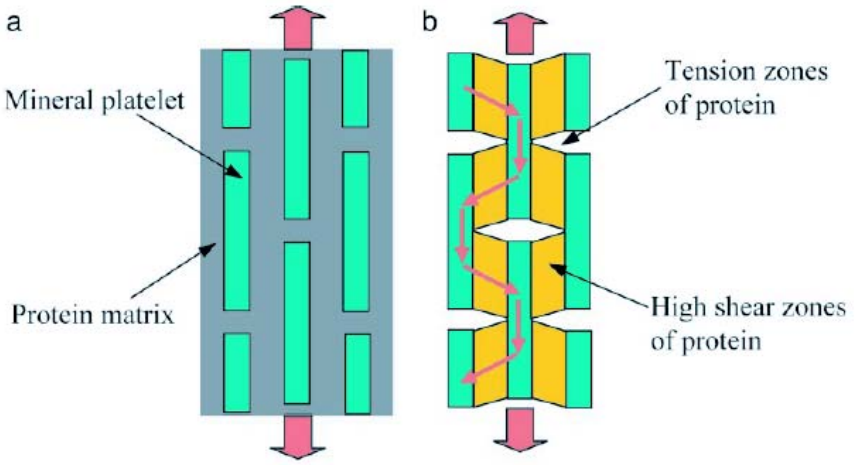

Figure 5-12: Staggered particle model of Jager and Fratzl [2000] and Gao et al [2003]

In the current investigation it was demonstrated that a large range of effective elastic modulus values could occur for composites with the same mineral volume fraction but different continuous phases, particle geometries, and particle distributions (Figure 5-7 (a) and (b)). These differences in composite structure, which lead directly to differences in effective modulus, may present one mechanism via which the steep changes in experimentally-measured bone modulus with mineral fraction (Figure 5-1) could be explained. The data from Figure 5-7(b) are plotted in Figure 5-13, illustrating the fact that the modulus indeed spans the H-S bounds at constant volume fraction mineral based on the particle aspect ratio and which phase is continuous. This is one factor that may help examine the observed bone data, and demonstrates clearly that Katz [1971] was correct in that mineral volume fraction alone is not sufficient to allow for the prediction of bone elastic modulus. However, with additional geometrical input (especially the interparticle spacing) the modulus can be predicted. Current information on bone ultrastructure does not definitively establish the stiffening mechanism of bone, but does suggest that high aspect ratio particles result in unphysically anisotropic behavior when considered in isolation. However, clues are contained within these examinations to suggest how discrete bone particles with high aspect ratios might combine to form a

structure that is essentially a “stiff phase continuous” mineral network, in that the interparticle spacing of adjacent mineral particles could be extremely small. This will be discussed further in section 5.7 later in this chapter.

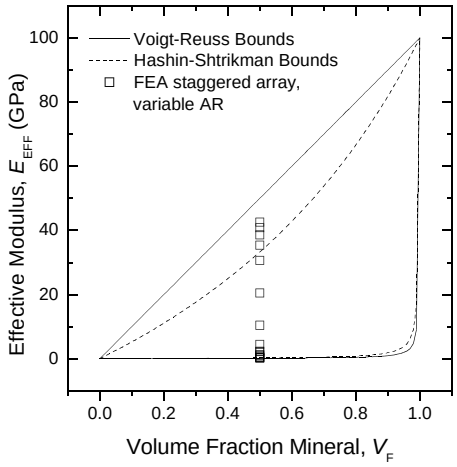

Figure 5-13: Comparison of composite bounds (E_{min} = 100 GPa and E_{coll}= 100 MPa) and finite element results for a staggered particle array, with varied continuous phase, particle aspect ratio, and particle orientation but fixed mineral volume fraction (all data points from Figure 5-7b).

5.4 Modeling of Interpenetrating Phase Composites

The modeling results from section 5.2 and 5.3 suggest that the stiff, apatite phase may be effectively continuous and that this may be necessary for the material of 50-50 volume fraction hydroxyapatite-collagen to attain an elastic modulus of 25 GPa with a transverse modulus also in the GPa range. It is widely accepted that the collagen network in bone is highly cross-linked and itself forms a 3D network that remains when the mineral phase is removed by demineralization in EDTA [Catanese et al, 1999]. This organic network can be tested in tension and has maximum elastic modulus values just prior to failure in the range of several hundred MPa (consistent with the use in this work of E = 100 MPa at small strains). Recently Hellmich and Ulm [2002] suggested that the mineral phase of bone is instead the continuous phase, and in doing so seemed to discount the existing evidence for collagen network crosslinking. This idea of bone mineral phase continuity is consistent with the microscopy results of Benezra Rosen et al [2002]. Finally, the observations of Gray [1901] as quoted in section 1.2.2.3 also suggest co-continuous networks in that something remains in the original shape of the bone when the other (protein or mineral) phase is removed through chemical means.

Recent finite element analysis on engineering materials with interpenetrating phases has been performed [Wegner and Gibson, 2000] and was used as a basis in the current work to model bone as a 3D two-phase interpenetrating phase composite. Extremely simple unit cell models were constructed in two geometries, (i) as a cube-in-cube system representative of single phase continuity (Figure 5-14(A)) and (ii) a two-phase co-continuous system with cubic elements of each material stacked like building blocks in layers to generate connectivity in all three dimensions (Figure 5-14(B)). Each model was constructed twice such that the phases were reversed in each second model. As above (section 5.2) all results were quantitatively evaluated by comparison with the same loading conditions on a homogeneous cube of E = 100 GPa to establish the effective elastic modulus of the composite. The homogeneous cube was also checked to verify numerical stress-strain results compared to analytic calculations for the same

loading conditions.

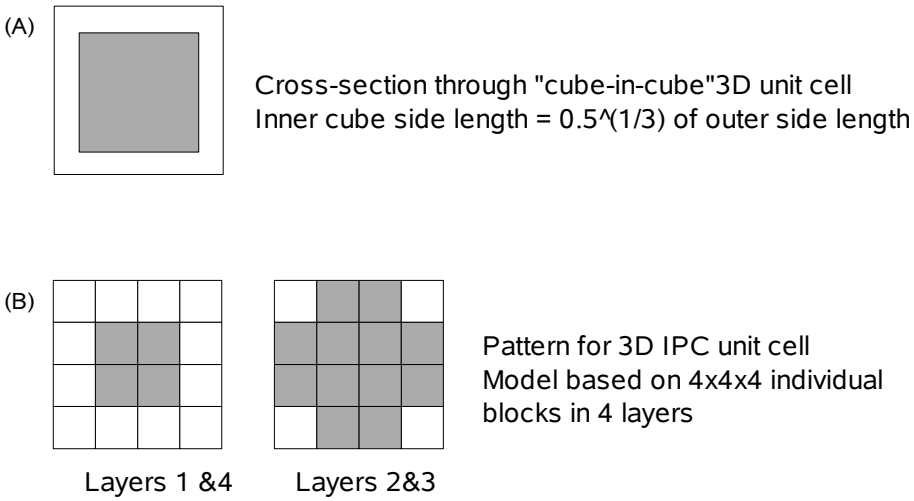

Figure 5-14: (A) Cube-in-cube model with 50% of each phase by volume; the outer layer is continuous while the shaded layer is a discrete particle. (B) Isotropic, 50-50 pattern of cubic elements in 2D layers combined in 3D by layer stacking to form two-phase interpenetrating phase composite. For both models, E_W is the modulus of the white phase and E_G is the modulus of the shaded phase.

Results are summarized in Table 5-6. As in previous 2D models, any model with a stiff continuous phase had an effective composite modulus approximately equal to the upper Hashin-Shtrikman bound. The single continuous phase model with a compliant continuous phase again resulted in a very low (<500 MPa) composite modulus.

Table 5-6: 3D Unit cell FEA results for the structures of Figure 5-14.

# continuous phases	E_W	E_G	E_{EFF}
1 (Fig. 5-14A)	100 GPa	100 MPa	35.7 GPa
1 (Fig. 5-14A)	100 MPa	100 GPa	477 MPa
2 (Fig. 5-14B)	100 GPa	100 MPa	29.8 GPa
2 (Fig. 5-14B)	100 MPa	100 GPa	28.7 GPa

The results are consistent with the two-dimensional modeling work presented in earlier sections, in that the single necessary condition for a bone-like elastic modulus under these conditions ($E_{collagen}$ = 100 MPa, $E_{mineral}$ = 100 GPa) is a continuous stiff phase.

There is no real difference between the one- and two-phase continuous models as long as the stiff phase is the continuous phase in single-phase continuous models. There is also no real difference between 2D and 3D models for homogeneous uniaxial loading. The results from earlier simulations, such as the effect of particle aspect ratio (section 5.3) can therefore be simply extrapolated from 2D into 3D. Therefore, the remainder of modeling presented in the current work will be performed in two dimensions (2D).

5.5 Porosity and Collagen Modulus Effects

In the extreme case of low modulus compliant phase, there is an obvious comparison between the composite structure and a porous foam material in which the compliant phase is nothing at all. The suggestion has been made that bone mineral behaves as a porous open cell foam [Hellmich and Ulm, 2002]. For open-cell foams, the modulus of the foam E_{foam} is given as [Gibson and Ashby, 1997]:

$$\frac{E_{\text{foam}}}{E_{\text{S}}} = \left(\frac{\rho_{\text{foam}}}{\rho_{\text{S}}} \right)^2 \qquad [5\text{-}13]$$

where the subscript "S" is for the fully dense solid. This expression would predict a modulus of 25 GPa for bone based on a hydroxyapatite skeleton with 50% volume fraction and an elastic modulus of 100 GPa. This value is comparable to both the elastic modulus bone, and also to the upper H-S limit of 33 GPa when the collagen modulus is 100 MPa. In the case of either a porous network or Hashin-Shtrikman composite model, clearly a fully continuous hydroxyapatite phase could single-handedly provide the elastic stiffness in bone. Experimental evidence supports the idea of a functional bone mineral matrix, as the elastic modulus of bone does not change after heating bone to temperatures sufficiently high for collagen denaturation [Wang et al, 2001]. However, other material properties, such as creep response and fracture toughness, may still be dependent on the collagen network to varying degrees.

This idea, of hydroxyapatite-only dependence of the elastic modulus, was evaluated with the 3D finite element models of the previous section, where the second phase was considered void (Figure 5-15). Results are presented in Table 5-7, demonstrating that in fact the collagen at 100 MPa is indeed contributing nothing to the elastic stiffness of the solid.

Table 5-7: Comparison of models in Figure 5-14 for compliant collagen compared to a void phase.

# continuous phases	E_W	E_G	*Ecomposite*
1	100 GPa	100 MPa	35.7 GPa
1	100 GPa	void	35.3 GPa
2	100 GPa	100 MPa	29.8 GPa
2	100 GPa	void	28.9 GPa

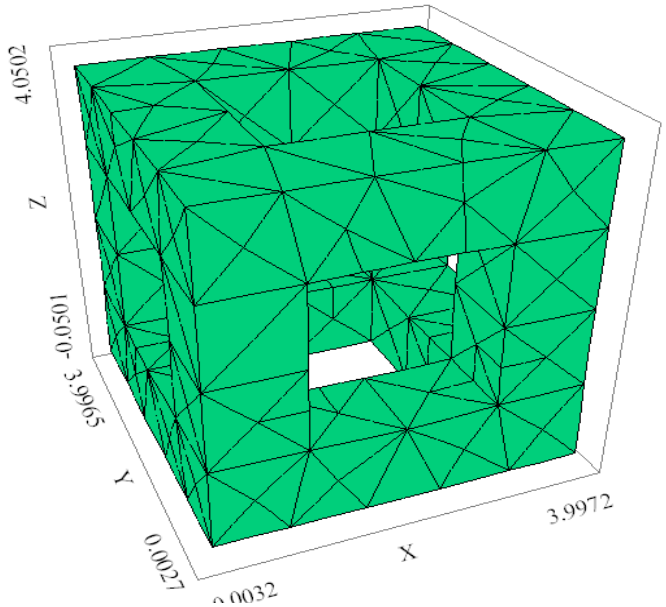

Figure 5-15: 3D rendering of 2-phase IPC FE model with one phase void

Since there was approximately no difference between the models with stiff continuous phases when the second phase was void or had a small but finite modulus (100 MPa), a closer examination of the Hashin-Shtrikman bounds was made for varying compliant-phase modulus at fixed stiff phase modulus of 100 GPa. For large modulus mismatch composites, while the upper H-S bound is relatively insensitive to the compliant phase modulus over a large range of values, conversely the lower H-S bound is relatively insensitive to the stiff phase modulus over a large range of values (Figure 5-16, left). It is noted that the compliant phase modulus does not substantially affect the upper

bound until this modulus is 2% or more of the stiff phase modulus (Figure 5-16, right). A limit of around 33 GPa was found for the upper bound when E_1 approaches 0 and E_2 = 100 GPa at 50% mineral volume fraction.

In general, then, porosity in the material only affects the modulus of bone or bone-like materials in that it restricts the amount of high-modulus mineral present to contribute to the elastic stiffness of the solid. Void phase and collagen phase can be more or less neglected in calculations of the solid modulus when a fully-connected mineral network is present.

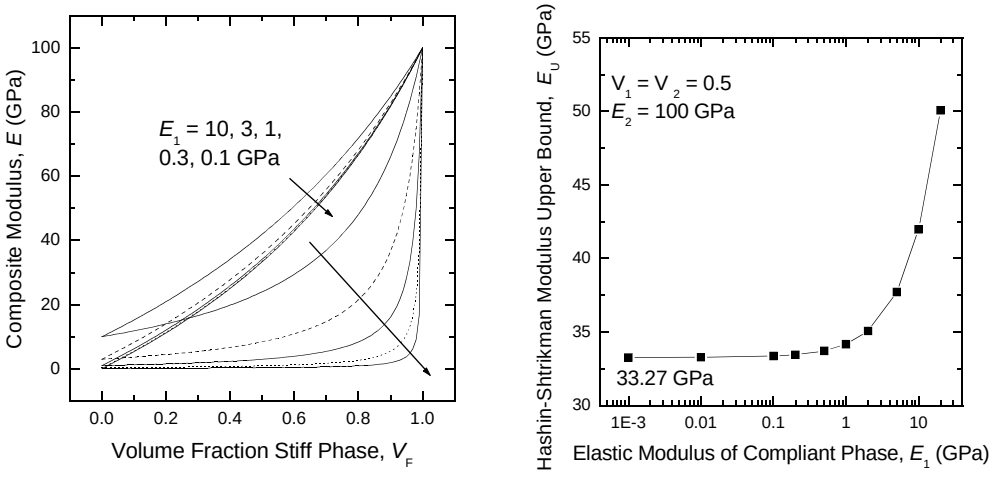

Figure 5-16: (left) Effect of compliant phase modulus on Hashin-Shtrikman bounds for a stiff phase with *E* = 100 GPa and compliant phase with varying modulus. (right) Effect of compliant phase modulus on Hashin-Shtrikman upper bound for a 50-50 mixture of stiff phase with *E* = 100 GPa and compliant phase with varying modulus.

5.6 Intermediate Connectivity

In addition to variations in particle aspect ratio and particle arrangement, another potential variable in constructing bone ultrastructural models is the connectivity of the phases. As shown above, the stiff phase perfectly continuous or perfectly noncontinuous in the direction of loading corresponds directly with the upper and lower bounds: Hashin-Shtrikman bounds for particle reinforced composites; Voigt-Reuss bounds for fiber-reinforced composites (Figure 5-17).

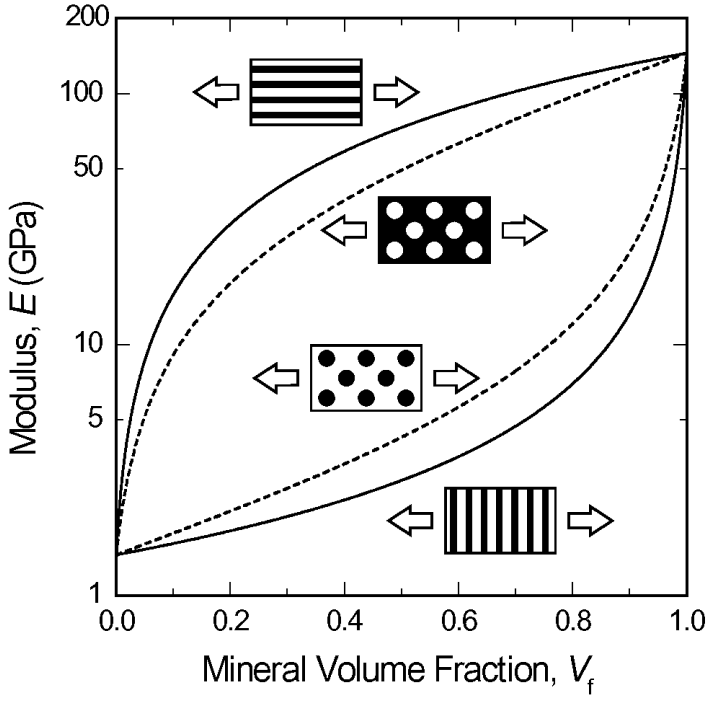

Figure 5-17: Schematic illustration of the V-R (solid) and H-S (dashed) modulus bounds along with the structures represented by the bounds, in which the stiff phase is the dark phase and the compliant phase is the light phase.

A potentially interesting configuration in bone, and one that would be consistent with the observations of Katz [1971] (Figure 5-1) would be mineral that is somehow "partially continuous". This idea has little bearing on most engineering composites, in which discrete reinforcement phases are added to a continuous matrix. However, in

mineralized biological tissues, the mineral accumulates on the collagen network via a process of nucleation and growth. Growth of mineral particles to the point that they begin to fuse is a not unrealistic way of considering mineralized tissues; it is well known that in dentin discrete lumps of mineral particles called calcospherites do fuse to form mineral superstructures with dimension of 10s of micrometers [Currey, 2002].

Recent finite element analysis studies on interpenetrating phase (co-continuous) engineering composites have shown a leap from the lower Hashin-Shtrikman modulus bound to the upper bound over a very narrow range of stiff-phase volume fraction when the stiff phase shifts from just-discontinuous to just-continuous [Wegner and Gibson, 2000]. This is could be possible in bone as well; at a critical mineral volume fraction the mineral phase could consolidate to a continuous porous network. This is another potential explanation for the data in Figure 5-1, and will be explored here specifically within the context of bone. Finite element models were constructed to examine the idea of partial mineral connectivity.

5.6.1 Intermediate Connectivity in 1D

A simple composite consisting of stiff fibers in a compliant matrix can be adapted to model partial connectivity in 1D. The fibers were interrupted in the center of the model, such that varying number of fibers were continuous across the load-bearing faces of the model and capable of providing reinforcement. By merely "breaking" the fibers for a short distance in the center of the model instead of completely removing them, this change in connectivity can be examined at nearly constant stiff-phase volume fraction. The fully "broken" fiber model is thus analogous to a model with high aspect-ratio discrete reinforcing particles, as was illustrated above in section 5.3. A schematic illustration of these models is presented in Figure 5-18 for a model with 5 possible fiber connections.

A broken fiber model with 15 total fibers and a reinforcement volume fraction of just under 0.5 was constructed in 2D plane strain using FlexPDE. Models were loaded in

tension homogeneously in the direction of the fibers by applying an equal and opposite displacement perturbation to each end. The number of connected fibers was varied from 0 to 15, taking care to "break" fibers symmetrically with respect to the centerline of the model. The total width of the model was 60 units, the length of each fiber segment on each side of the centerline was 28 units, and each fiber connector in the center was 4 units in length. The effective modulus of the composite was calculated as above (section 5.2). For the case when 0 connections were present, the modulus could be predicted with the "length fraction" argument as presented above (section 5.3.3); the total L_p was 56/60 = 0.93, giving a predicted modulus from the lower V-R bound of 1.41 GPa from Eqn. 5-12. The value from the finite element model was 1.53 GPa. (and compared with a lower V-R bound value of 0.19 GPa based on volume fraction alone without the length fraction consideration).

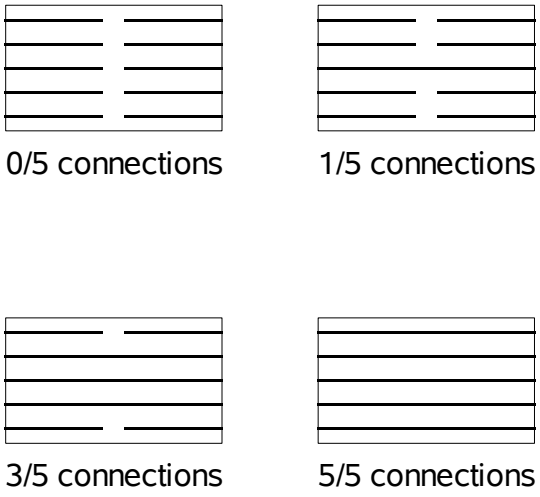

Figure 5-18: Interrupted fiber model for examining partially connected composite materials with nearly constant volume fraction of reinforcement phase.

These modulus results are shown in Figure 5-19. The modulus varies from just above the lower V-R bound (as discussed above) to approximately equal to the upper V-R bound at nearly constant volume fraction reinforcement phase (Figure 5-19).

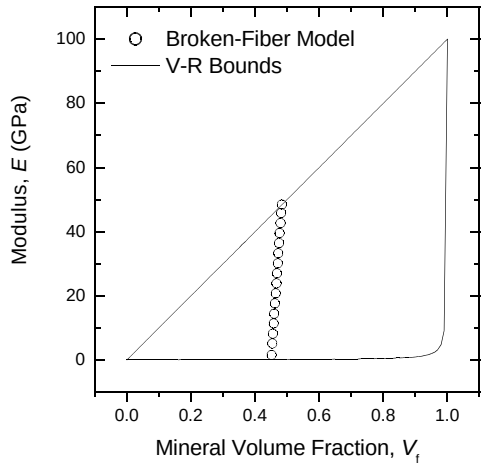

Figure 5-19: Elastic modulus values for the interrupted fiber model as compared with the Voigt-Reuss composite bounds. The model values span the bounds at nearly constant volume fraction based on different levels of partial connection.

From the "broken fiber" model geometry, a volume fraction of "connected phase" $(V_{\mathrm{f}}^{\mathrm{cxn}})$ can be calculated separate from the total volume fraction of reinforcement phase by only including the continuous fibers as reinforcement in the calculation $V_{\mathrm{f}}^{\mathrm{cxn}}$ volume of connected fibers divided by the total volume. A geometrical connectivity fraction (F^{cxn}) for the reinforcing phase can then be computed objectively, as the ratio of connected volume (or volume)fraction to total volume (or volume fraction) reinforcement:

$$F^{\mathrm{cxn}} = \frac{V_{\mathrm{f}}^{\mathrm{cxn}}}{V_{\mathrm{f}}} = \frac{v_{\mathrm{f}}^{\mathrm{cxn}}}{v_{\mathrm{f}}} \qquad [5\text{-}14]$$

It was hypothesized that the connection fraction could be estimated by simple scaling of the modulus results for the partially connected phase with the modulus values of the upper and lower bounds for a material with the same total volume fraction reinforcing phase, illustrated schematically in Figure 5-20. This scaling can be expressed as

$$F^{\text{cxn}} = \frac{E - E^{\text{L}}(V_{\text{f}})}{E^{\text{U}}(V_{\text{f}}) - E^{\text{L}}(V_{\text{f}})} \qquad [5\text{-}15]$$

where E is the observed modulus, $E^{\text{L}}(V_{\text{f}})$ is the lower bound value for the same mineral volume fraction (V_{f}), and $E^{\text{U}}(V_{\text{f}})$ is the upper bound modulus value for the same mineral volume fraction. For large modulus mismatch $(E^{\text{U}} \gg E^{\text{L}})$ this can be approximated by

$$F^{\text{cxn}} = \frac{E - E^{\text{L}}(V_{\text{f}})}{E^{\text{U}}(V_{\text{f}}) - E^{\text{L}}(V_{\text{f}})} \approx \frac{E}{E^{\text{U}}(V_{\text{f}})} \qquad [5\text{-}16]$$

For the broken fiber model, the appropriate upper and lower bounds to consider are the Voigt-Reuss bounds.

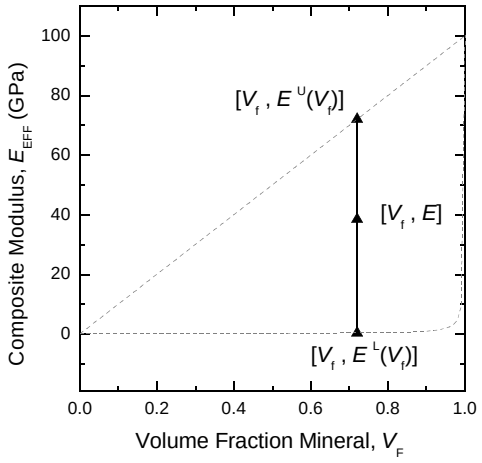

Figure 5-20: Illustration of the parameters used to estimate connectivity from elastic modulus.

It was indeed found that this approximate calculation of F^{cxn} based on the elastic modulus results did approximate the true geometric connected phase fraction for all different connectivities of the broken fiber model (Figure 5-21). Since the model utilized the three order of magnitude modulus mismatch used frequently throughout this work (E_1

= 100 MPa, E_2 = 100 GPa), the simple approximation based on the upper bound only (Eqn. 5-16) was found to be no different than Eqn 5-15 and thus the simpler form was used.

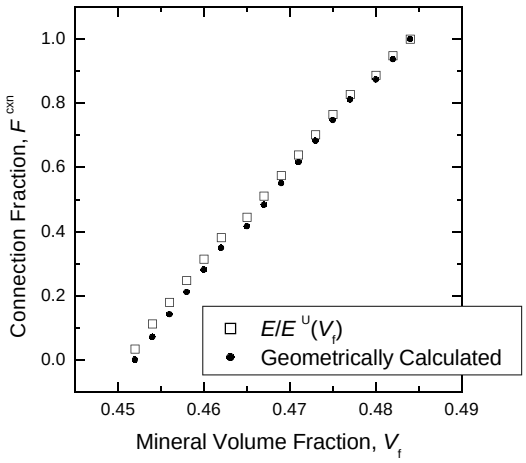

Figure 5-21: Comparison of the connectivity fraction (F^{cxn}) calculated directly from the model geometry and estimated from the elastic modulus value. The two compare favorably over the range of observed behaviors.

Given the low anisotropy in bone (certainly compared to that caused by one-dimensional fiber reinforcement), this model was considered to be an oversimplification of the processes that could be happening in bone structure, and a more physically-realistic two-dimensional model was sought.

5.6.2 Intermediate Connectivity in 2D

The effect of phase intermediate connectivity in more than one dimension was examined using a finite element mesh with three distinct elements: (1) stiff particles, (2) a compliant matrix, (3) stiff bridging connectors between different particles in two dimensions. This model framework is shown in Figure 5-22.

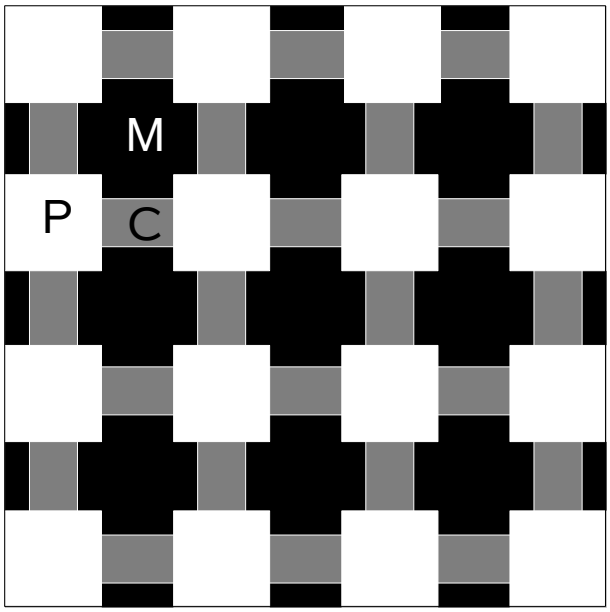

Figure 5-22: Three-component model with matrix (M), particles (P), and inter-particle connectors (C).

The width of the connectors was fixed at half the particle dimension (*P*/2) and their length (e.g. the particle-to-particle distance) was varied to give variations in volume fraction stiff (apatite) phase. Each connecter was either present or absent in any given model, and was typically assigned the same elastic modulus as the particles (but could also be assigned an intermediate modulus value if desired). The configuration utilized in the current work consisted of 16 particles (as shown in Figure 5-22), and a total of 24 connecting bridges, 12 each in the *x*- and *y*-directions. For this 16-particle configuration, the ranges in volume fraction depending on the interparticle spacing (bridge length) and number of connecters present is in Table 5-8, where zero connecters corresponds to a compliant phase continuous model with individual discrete particles and all connecters present correspond to a stiff phase continuous model with isolated pockets or particles of compliant phase. A model with interparticle spacing set to the particle size gave a range of volume fraction values corresponding to those for bone (varying around 0.5, Table 5-8).

Table 5-8: Volume fractions of mineral for models with different interparticle spacing (*p*) and numbers of physical connecters

Interparticle spacing, multiples of particle size, p	*0 connecters present*	*Half of connecters present*	*All connecters present*
0.2	0.76	0.81	0.87
0.5	0.53	0.63	0.73
1	0.33	0.45	0.57
2	0.16	0.28	0.4
5	0.04	0.13	0.21

For this model in two-dimensions, there are now two critical descriptors of the phase connectivity, one in each direction (here denoted "Cx" and "Cy"). Schematic illustrations of the models for fully connected (Ci = 1) and fully detached (Ci = 0) bridges or linkages in each direction are shown in Figure 5-23.

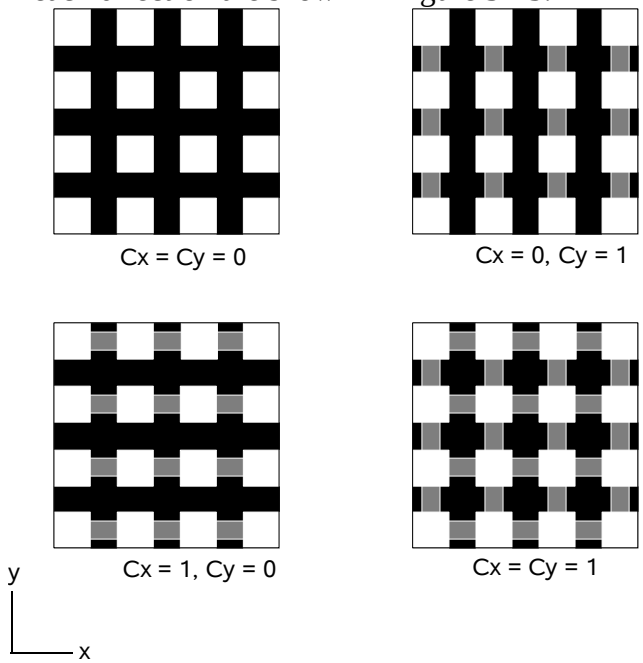

Figure 5-23: Schematic illustration of connectivity indices, Cx and Cy in the *x*- and *y*-directions, respectively.

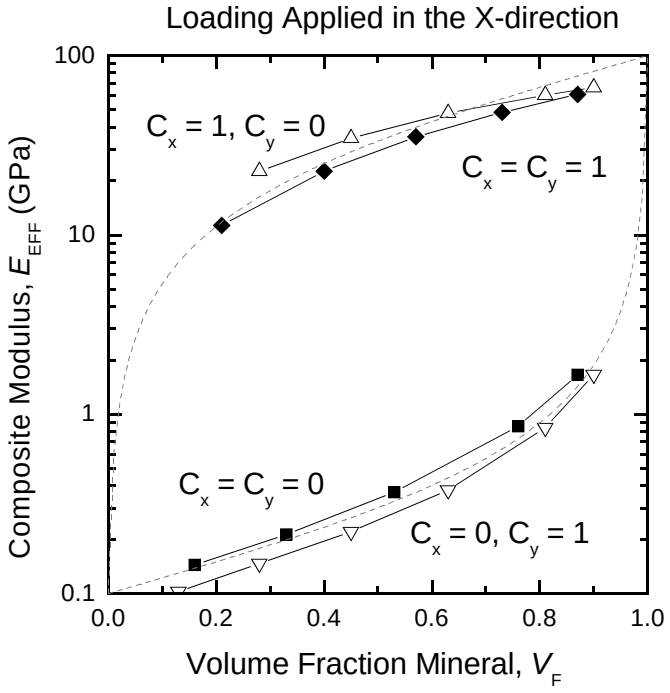

Figure 5-24: Composite modulus results for the four configurations shown above in Figure 5-23. Consistent with earlier results, the loading direction is really important in determining overall behavior and the non-loading direction has almost no effect. Results are consistent with earlier sections in this chapter, in that stiff-phase continuity is associated with the upper H-S bound and stiff phase discontinuity is associated with the lower H-S bound (dotted lines)

Next partially connected structures were examined. The connection index was associated with direct paths across the model, as illustrated in Figure 5-25. In this simple model of sixteen particles, (Figure 5-22) there are four direct paths across the model in one direction, corresponding to the four rows or columns of particles. Therefore intermediate connectivities of Cx = 0.25, 0.5, or 0.75 are possible (Figure 5-25).

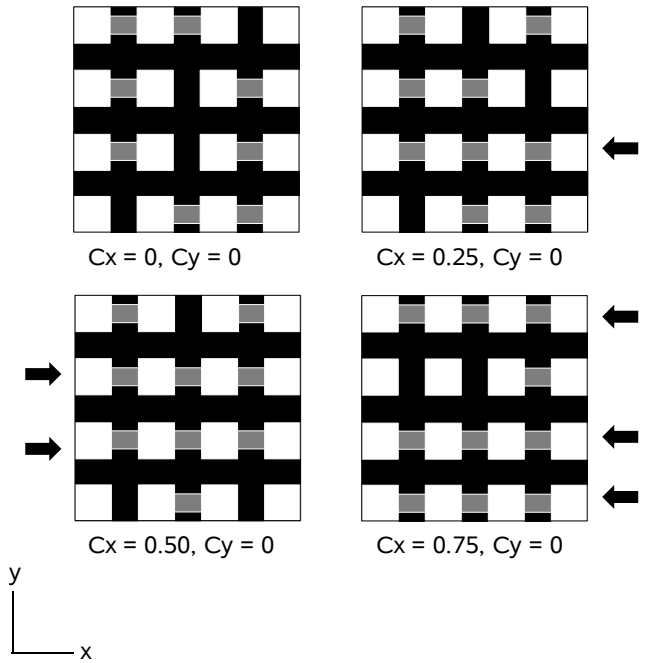

Figure 5-25: Schematic illustration of intermediate values of the connectivity indices Cx for intermediate connectivity values in the *x*-direction.

Two different mechanisms for discontinuity in any one row of particles were considered, as shown in Figure 5-26: (1) a single linkage was removed from the row; (2) whole rows of bridging connectors were removed at once for the entire row. The intermediate case (two of three linkages removed in a single row) was not considered in this series of models, as it represents an intermediate result.

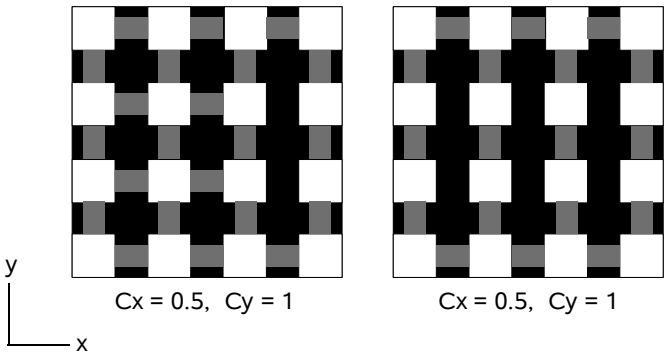

Figure 5-26: Intermediate connectivity models caused by the removal of (left) single linkages or (right) whole rows of linkages in the loading (*x*-) direction.

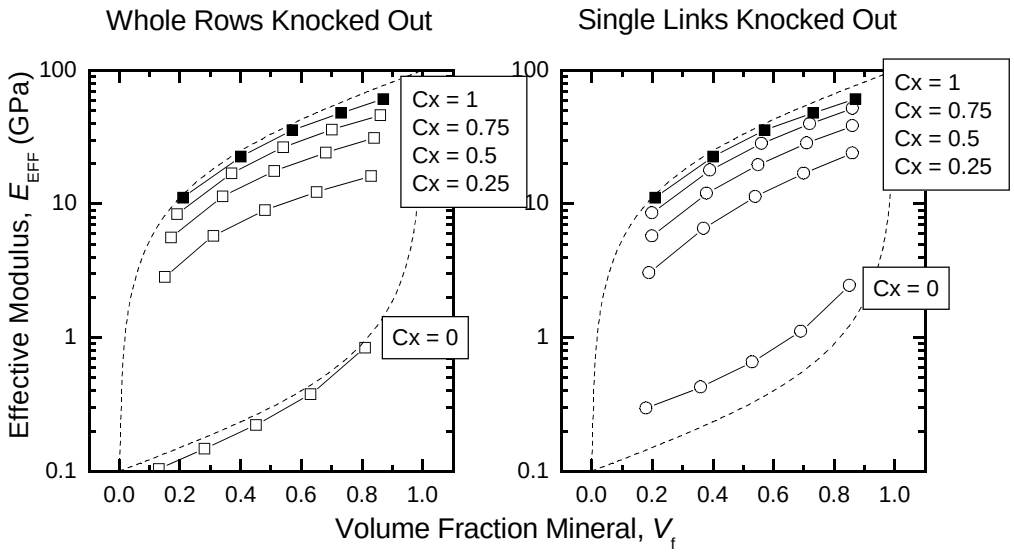

Figure 5-27: Variation in the composite modulus with mineral volume fraction for different fractions of connected paths across the structure in the direction of loading. Intermediate connectivity fractions were established by (left) removal of whole rows of connectors and (right) removal of single connectors in each row. The transverse phase was fully connected (Cy = 1).

Results for effective modulus as a function of mineral volume fraction are shown in Figure 5-27 for intermediate connectivity models in different configurations. Results for removal of entire connector rows and single connectors are similar, except in the case of Cx = 0 where removal of single connectors only resulted in a slightly higher modulus compared to removal of entire connector rows. In both cases, there is a large jump in modulus from Cx = 0 to Cx = 0.25 and further increases for each increase in connection fraction (Cx). For partially connected models (Cx = 0.25, 0.5, 0.75) the trends with volume fraction were parallel to the upper H-S bound (dashed lines) and concave down, while for Cx = 0 the trend was concave up and parallel to the lower H-S bound.

The connectivity fraction was estimated from the elastic modulus results shown in Figure 5-27, and compared to the known Cx values. The connectivity fraction was calculated from the modulus value by scaling the modulus to the upper H-S bound

modulus for same mineral volume fraction (Eqn. 5-16). Results are shown in Figure 5-28 for the data presented in Figure 5-27, for both whole rows of connectors removed and single linkages removed. There is good agreement between the estimates and the known geometrical connectivity for most mineral volume fractions and connectivity values, with greatest discrepancies seen at high volume fraction or high (unity) connectivity. Thus, this simple estimate of the geometrical connectivity of a structure, based on the scaling of elastic modulus and as derived for broken fiber composites (section 5.6.1) is effective in providing a first order estimate of the structural connectivity.

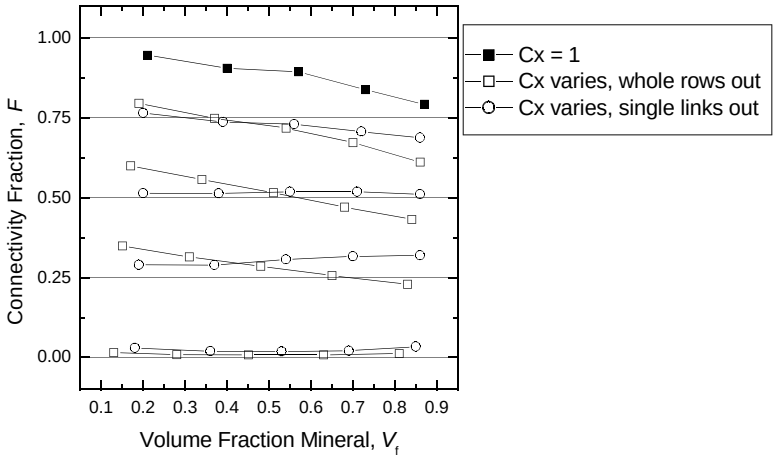

Figure 5- 28: Calculated connectivity fraction for the data shown in Figure 5-26, based on the modulus scaling of Eqn. 5-16. The solid lines represent the connectivity based on the fraction of connected paths (out of 4) in the structure.

Modulus data for fixed interparticle spacing (equal to the particle size, *P*) and different connectivity values are shown in Figure 5-29 for the data taken from Figure 5-27. In drawing lines for approximately fixed volume fraction but different connectivities, (instead of fixed connectivity at different volume fractions, Fig. 5-27) a steep trend in bone modulus with mineral volume fraction (Figure 5-1) can be explained by a change in phase connectivity.

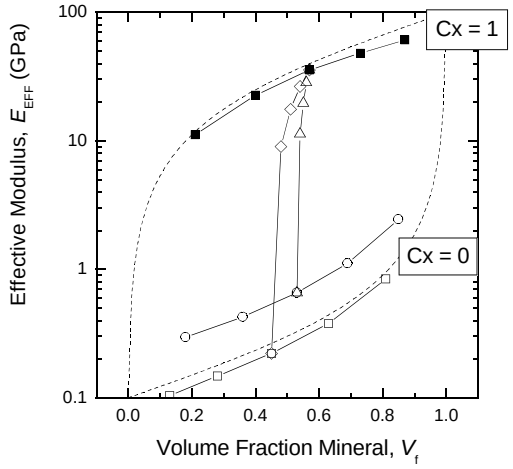

Figure 5-29: Variation in the composite modulus with mineral phase connectivity at near-constant volume fraction. Data are a subset of that presented in Figure 5-27 for interparticle spacing equal to the particle size and both single linkages and whole rows removed. The trends are similar, to steeply increasing modulus with small changes in mineral volume fraction.

Next the effect of both transverse phase connectivity and precise details of structural arrangement were examined in a partially-connected model in which all or none of the transverse connections were present (Cy = 0 or 1) and in which two thirds (8/12) x-direction connectors were present, giving rise to values of Cx = 0, 0.25, or 0.5. Every possible configuration of the eight x-direction connectors was examined (Figure 5-30) and a naming scheme was established to uniquely describe each structure, as shown in Fig. 5-30. The results were compared to models with fully connected (Ci = 1) and fully disconnected (Ci = 0) phases in each direction.

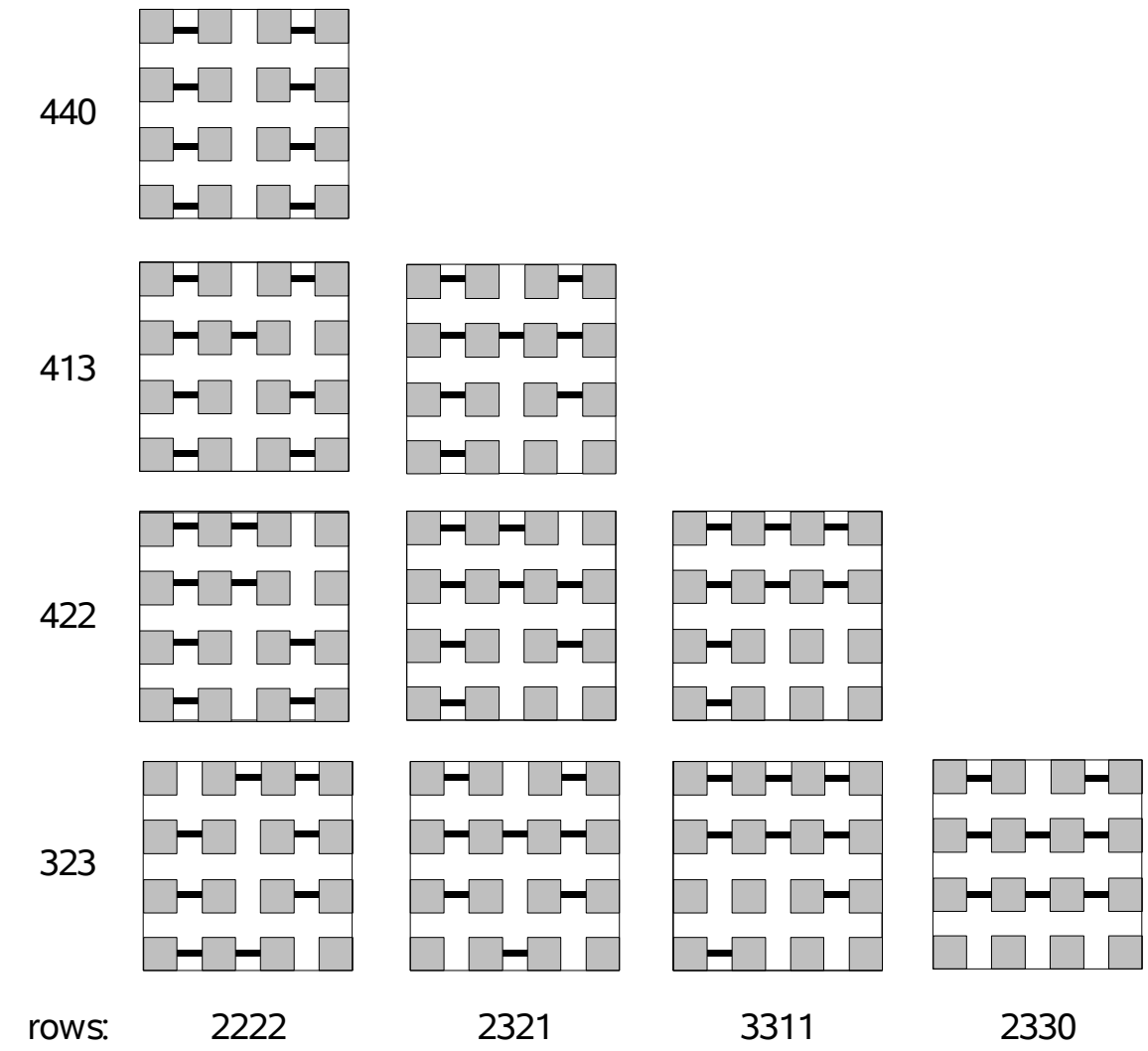

Figure 5-30: A series of partially-connected composites with 8/12 linkages in the *x*-direction arranged in all possible configurations. The geometrical designators uniquely describing each individual configuration are given, as per the number of connections in each row or column.

Results for the effective elastic modulus of the structures shown in Figure 5-30 are presented in Table 5-9. For comparison, the completely connected (444-3333) material the effective modulus was 35.15 (Cy=1) or 34.80 (Cy=0) GPa, and for the unconnected material (000-0000) the effective modulus was 0.24 (Cy=1) or 0.21 (Cy=0) GPa. The 2D model has behavior dominated by the number of complete, direct paths of

reinforcement across the material, as characterized by the Cx value. Details of the organization of these connections has little effect on modulus results when compared to the dramatic effects of the Cx value except in the case of Cx = 0.

Table 5-9: Effective elastic modulus results for the partially-connected structures shown in Figure 5-30

Modulus, E (GPa)	***2222 (Cx = 0)***	***2321 (Cx = 0.25)***	***3311 (Cx = 0.5)***	***2330 (Cx = 0.5)***
440: Cy=1 Cy=0	0.71 0.63			
413: Cy=1 Cy=0	3.72 0.66	10.21 9.07		
422: Cy=1 Cy=0	1.90 0.64	10.05 9.09	18.05 17.6	
323: Cy=1 Cy=0	4.50 0.71	9.52 9.06	17.94 17.50	18.06 17.54

The effect of transverse (Cy) connection on results for longitudinal (x-direction) loading only appears important in the case where there are zero direct paths across (the 2222 set, Cx = 0) and even then, the total effect is less than half the effective stiffening due to having at least one connected longitudinal path (Cx = 0.25).

For a bone-like elastic modulus in this model, about ½ to ¾ of all paths must be directly connected in the direction of loading. In fact, a bone-like anisotropy ratio along with bone-like elastic modulus values occur when ¾ of paths are connected in one direction (E_1 ~ 27 GPa) and ½ are connected in the other (E_2 ~ 18 GPa) giving E_1/E_2 = 1.5.

5.7 Discussion

In this chapter, a series of modeling exercises was performed to examine the effect of different proposed geometrical arrangements of bone mineral at the ultrastructural scale. In particular, the effects of particle aspect ratio and phase connectivity were explored. Comparisons were made with both the numerical values of bone moduli as well as with the observed anisotropy of bone, characterized by a longitudinal to transverse modulus ratio of approximately 1.5 [Hayes, 1991] to 1.75 [Swadener et al, 2001].

For enamel, the modulus-volume fraction data appear to lie along the lower bound (Figure 5-1), indicating discontinuous mineral platelets separated by a small amount of organic matter. The thickness of this layer could be estimated using the "particle length fraction" argument in each direction, as presented in section 5.3.3, along with detailed structural information about enamel prism geometry in the tooth of interest.

There is considerable evidence to support a very different microstructure for bone and dentin. Bone modulus spans the region between the composite bounds, and dentin seems to exist in a narrow region near the upper bound. The structural evidence for a continuous (or at least partially-continuous) mineral phase in bone and dentin goes back to observations published in Gray's anatomy a century ago, and probably substantially much further back than that (especially in France, where the art of making chicken stock is so crucial to the cuisine[*]). The GPa-range elastic modulus for a 50% mineral composite, along with the observed moderate anisotropy of bone, is far more easily justified with mineral phase continuity than with any proposed stiffening mechanism, such as high aspect-ratio particle stiffening [Jager and Fratzl, 2000; Gao et al, 2003]. Unfortunately, the pioneering work of Hellmich and Ulm [2002] in recognizing the mechanical arguments for mineral phase connectivity has gone largely unnoticed in most

* Alton Brown, of Food TV's "Good Eats" program, in describing the production of chicken stock illustrated the completion of the stock process by showing that the chicken bones remained intact, although whiter in appearance, but could now be broken easily and in a brittle manner since the connective tissue has been dissolved into the stock.

models of bone or dentin (although the work of Hellmich and Ulm neglects the collagen phase continuity, and thus the nature of bone as an interpenetrating phase composite). However, the connectivity of the mineral phase is supported strongly by the modeling work presented in the current chapter.

It is known from high resolution microscopy studies that individual bone mineral particles are high aspect-ratio, and yet the bone material itself is only relatively moderately anisotropic. Previous ultrastructural models for bone [Jager and Fratzl, 2000; Kotha and Guzelsu, 2002; Gao et al, 2003] incorporated isolated high aspect-ratio mineral particles in a compliant matrix, a configuration that produces far more structural anisotropy than is observed in bone. A question can also be raised as to the mechanical stability of isolated high aspect-ratio mineral platelets, particularly in bending or buckling conditions.

A simple structural model to demonstrate one manner in which these two apparently opposing facts, the high aspect ratio of individual mineral crystals and the small anisotropy observed in bone, can be reconciled is presented in Figure 5-31. The individual particles (with AR = 16) are closely opposed laterally, and could be joined either by thin layers of organic or inorganic material to keep this joined mineral "matrix" sufficiently stiff and comparable to a homogeneous continuous phase. This structure has some similarities to the "prism" structure found in enamel, in which the extremely high-AR mineral particles fuse laterally to form "prism" structures, and the protein phase is concentrated at inter-prism boundaries instead of between individual mineral crystals (section 1.2.3.1). Clearly further ultrastructural microscopy and examination of bone and allied materials will be required in order to establish the details of the organization of mineral crystals at nm scales. However, the current work provides some suggestions as to what probably is not happening, particularly arguing against isolated action of high aspect ratio particles.

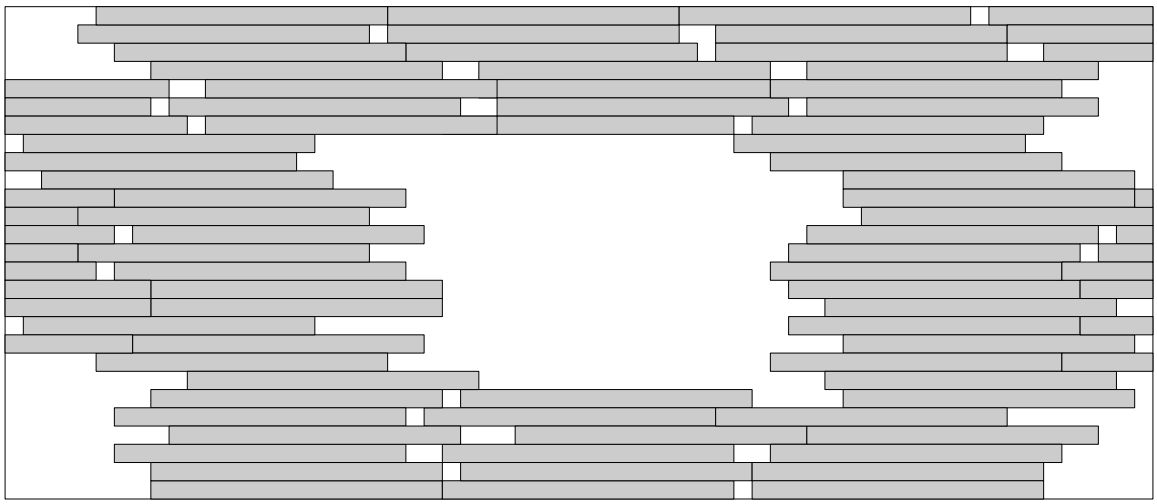

Figure 5-31: A proposed structural model of bone based on the observed mineral particle geometry (high aspect-ratio) but in which the overall anisotropy of the structure is reduced by groups of mineral particles forming an effective stiff "continuous matrix". These groups are organized to effectively have structural elements with no more than an aspect ratio of 2 remaining in the structure.

In bone, large variations in elastic modulus have been observed at approximately constant mineral volume fraction, as shown schematically in Figure 5-1. The modulus of bone thus spans the region between the upper and lower bounds for composite behavior. Two different illustrations of this type of behavior were generated in the current work, demonstrating the effects of changing particle aspect ratio in Figure 5-13 and changing phase continuity in Figure 5-29. In both of these figures (5-13 and 29) the effect seen in bone is replicated, in which ***structural*** variations in the geometrical organization at fixed or nearly fixed composition (volume fraction mineral) give rise to modulus values that span the range between the composite bounds. Given the fact that the mineral particles found in bone are reasonably uniform in size and shape (probably for very good thermodynamic reasons) the aspect ratio variations probably play a minor role in causing the effect seen in bone, while variations in the phase connectivity could certainly dominate. Again, there is a clear motivation here for further examination of the mineral structure at nanometer and sub-nm length-scales.